Controlled lateral anisotropy in correlated manganite heterostructures by interface-engineered oxygen octahedral coupling

Z. Liao[1], M. Huijben[1*], Z. Zhong[2], N. Gauquelin[3], S. Macke[4,5], R. J. Green[4,6], S. van Aert[3], J. Verbeeck[3], G. Van Tendeloo[3], K. Held[2], G. A. Sawatzky[4], G. Koster[1] & G. Rijnders[1]

[1]*MESA+ Institute for Nanotechnology, University of Twente, P.O.BOX 217, 7500 AE, Enschede, The Netherlands*

[2]*Institute of Solid State Physics, Vienna University of Technology, A-1040 Vienna, Austria*

[3]*Electron Microscopy for Materials Science (EMAT), University of Antwerp, 2020 Antwerp, Belgium*

[4]*Quantum Matter Institute and Department of Physics and Astronomy, University of British Columbia, 2355 East Mall , Vancouver, V6T 1Z4 , Canada*

[5]*Max Planck Institute for Solid State Research, Heisenbergstraße 1, 70569 Stuttgart, Germany*

[6]*Max Planck Institute for Chemical Physics of Solids, Nöthnitzerstraße 40, 01187 Dresden, Germany*

Ultimate miniaturization of magnetic random access memory (MRAM) devices is expected by the utilization of spin-transfer torques, because they present an efficient means to switch elements with a very high magnetic anisotropy[1,2]. To overcome the low switching speed in current collinearly magnetized devices, new routes are being explored to realize magnetic tunnel junction stacks with non-collinear magnetization between two magnetic electrodes. Controlled in-plane rotation of the magnetic easy axis in manganite heterostructures by tailoring the interface oxygen

---
[*] email: m.huijben@utwente.nl

network would provide a promising direction for non-collinear magnetization in correlated oxide magnetic tunneling junctions. Here, we demonstrate how to manipulate magnetic and electronic anisotropic properties in manganite heterostructures by engineering the oxygen network on the unit-cell level. The strong oxygen octahedral coupling is found to transfer the octahedral rotation, present in the $NdGaO_3$ (NGO) substrate, to the $La_{2/3}Sr_{1/3}MnO_3$ (LSMO) film in the interface region. This causes an unexpected realignment of the magnetic easy axis along the short axis of the LSMO unit cell as well as the presence of a giant anisotropic transport in these ultrathin LSMO films. As a result we possess control of the lateral magnetic and electronic anisotropies by atomic scale design of the oxygen octahedral rotation.

Emergent phenomena in oxide heterostructures[3,4] such as interface charge transfer[5], two dimensional free electron gas[6] and ferromagnetism between two non-magnetic materials[7], are induced by the dedicated coupling between spin, orbital, charge and lattice degrees of freedom[8,9]. Developing strategies to engineer these intimate couplings in oxide heterostructures is crucial to achieve new phenomena and to pave the path towards novel functionalities with atomic scale dimensions. Utilizing polar discontinuity[6], inducing strain[10-12], charge transfer[5], and spatial confinement[13,14] are several well-known strategies. In ABO_3 perovskites orbital, charge and spin order are intimately correlated to the BO_6 oxygen octahedra[15-22]. In the bulk, the oxygen octahedral rotation (OOR) and deformation are usually controlled by isovalent substitution or by the deployment of high pressure[15-21], but oxide heterostructures offer additional ways to tune the lattice structure[3,4,12,22-26]. The OOR can be tailored either by strain or interfacial oxygen

octahedral coupling (OOC)[25-29]. The OOC is a geometric constraint effect which forces the octahedra in a film to rotate due to a retained corner-connectivity of oxygen octahedra across an interface[25].

For decades, strain has been used for heterostructure engineering, but strain is usually a long range effect depending on lattice mismatch[30] and therefore less controllable at the atomic scale, limiting its application towards complex devices where films with varying local properties on a single wafer are required. The OOC, which unlike strain has a short impact length scale of ~ 2 nm[25-29], could be a new route to realize atomic scale control of material properties and functionalities. However, the questions are still open whether the OOC can compete with strain, how strong of an impact it can make on the functionalities and if it can transfer not only the magnitude of rotation but also the Glazer rotation pattern[31] to a film. Such controllable OOR will provide a feasible new route to the artificial design of structures with novel functionalities.

By utilizing the OOC at the LSMO and NGO (110) interface, we demonstrate the possibility to transfer the characteristic NGO anisotropic structure into epitaxial LSMO films. This in turn creates not only new but also switchable magnetic and electronic anisotropies. The rhombohedral LSMO possesses an $a^-a^-a^-$ rotation which results in an isotropic B-O-B bond angle (θ) and isotropic properties[18]. The Glazer symbol[31] here and after is sequentially corresponding to the rotation along a, b and c axis respectively. In contrast, the orthorhombic NGO possesses an $c^+a^-a^-$ rotation with a larger θ along the [001] direction than along the [1-10] direction[32]. For convenience, pseudo-cubic indices are used for NGO with a, b and c corresponding to [001], [1-10] and [110] respectively. The structural characteristics of LSMO and NGO give rise to in-phase vs. out–of-phase

rotation type mismatch occurring along the *a*-axis (see left panel of Fig. 1a) while both are out-of-phase along the *b*-axis (see right panel of Fig. 1a). The magnitude of the bond angle θ also has a certain degree of mismatch: ~154 $^{\circ}$ in NGO vs. 166.3 $^{\circ}$ in LSMO. As a result, both the anisotropic rotation type mismatch and the large difference (~12°) in bond angle will cause a strong discontinuity of the octahedra (see Fig. 1a). Therefore, the oxygen atoms need to rearrange at the interface, resulting in a large change of the OOR in the LSMO film.

The effect of the OOC at the LSMO/NGO interface is visualized by atomically resolved Cs-corrected scanning transmission electron microscopy (STEM). Thin LSMO films with thicknesses ranging from 4 to 90 unit cells (uc) have been grown by pulsed laser deposition on NGO (110) substrates[33] (see Supplementary Fig. S1). All films are fully strained to NGO (See Supplementary Fig. S2), resulting an overall ~ 0.4% compressive strain on LSMO with 0.2% in-plane anisotropy[18,32]. The zone axis for the LSMO/NGO cross-section STEM specimen is chosen to be the *a*-axis due to its in-phase rotation, which allows us to resolve the oxygen atoms more easily[29,34]. Atomic resolution Energy-dispersive X-ray spectroscopy demonstrates the high-quality of the atomic ordering at the LSMO/NGO interface (See Supplementary Fig. S3). Annular Bright-Field STEM (ABF-STEM) was used to visualize the oxygen octahedra across the interface (inversed contrast for easier discernment of the individual atomic columns), as shown in Fig. 1b. The LSMO strongly follows the NGO rotation characteristic and becomes in-phase along the *a*-axis, which in bulk LSMO is out-of-phase. Close to the interface, the MnO_6 octahedral tilt angle is comparable to that of GaO_6, as shown by the depth profile of BO_6 tilt angle across the interface in Fig. 1c (For estimation of tilt angle, see Supplementary Fig. S4).

The tilt angle continuously changes from the GaO_6 substrate value to bulk MnO_6 (far from interface). Interestingly, the first 2 uc layers of LSMO have almost the same tilt angle as NGO. The impact of the octahedral coupling decays rapidly away from the interface and disappears above 4 uc layers. Therefore, the OOC at the LSMO/NGO interface results in the alteration of the OOR (in-phase, out-of-phase) of the LSMO close to the interface, in which the magnitude of the tilt angle is comparable to that of NGO, see left panel of Fig. 1b. Because of the short impact length scale of OOC, the OOR of the LSMO can be significantly altered by inserting a non-tilted $SrTiO_3$ (STO) buffer layer, see right panel of Fig. 1b. Within the STO layer, the OOR is also coupled to the OOR of NGO, but the tilt angle relaxes quickly, i.e., the tilt of TiO_6 octahedra starts to disappear above 2 uc layers. Consequently, the LSMO connects to a non-tilted OOR and doesn't show any evidence, within the STEM spatial resolution, of tilting of the MnO_6 octahedra from the first layer (see Fig. 1b-c). Together with non-buffered LSMO, the resulting interface structure of LSMO indicates that the local OOR at the substrate surface acts as a controllable template for the structure of the epitaxial LSMO film.

The observed interfacial OOC has a dramatic impact on the magnetic properties. The 9 uc STO buffer layer reduces the octahedral tilt in LSMO, thus enhances the magnetism, i.e., 9 uc STO buffer layer increases the Curie temperature (T_C) of the 6 uc LSMO from 145 K to 240 K. The enhancement is already found when using a 1 uc STO buffer layer as the 6 uc LSMO film exhibits a T_C of 180 K, indicating that 1 uc STO is thick enough to significantly reduce the octahedral tilt. The saturated magnetic moment of such STO-buffered LSMO is also larger than the non-buffered LSMO film (see Fig. 2a-c).

Beyond the enhancement, a more striking phenomenon is the switch of magnetic anisotropy (MA) by engineering the interfacial OOR. Due to the different OOR pattern, the 6 uc thick LSMO films with or without STO buffer layer have a different magnetization easy axis, although both exhibit uniaxial MA. The easy axis of the non-buffered LSMO is the *a*-axis as shown in Fig. 2a, in strong contrast to the observed *b*-axis easy axis in thick LSMO films[33,35]. When inserting a STO buffer layer with a thickness ranging from 1 uc to 36 uc (LSMO/STO/NGO) the easy axis is again switched to the *b*-axis. The magnetic behavior of 6 uc LSMO films on top of a 1 uc STO and 9 uc STO buffer layer is shown as example in respectively Figures 2b and 2c. For convenience, the MA with easy axis along the short axis *a* is defined as interfacial magnetic anisotropy (IMA) while an easy axis along the long axis *b* is indicated as bulk magnetic anisotropy (BMA). Comparison between the structure of LSMO with and without STO buffer layer indicates that the IMA is correlated to the strong tilted LSMO structure while the BMA comes from the nearly non-tilted (NNT) structure. Since the STO crystal is very stiff, the tilt angle is already strongly reduced within the first STO unit cell (see Fig. 1c). A single unit cell STO buffer layer is thick enough to switch the easy axis of LSMO, indicating the capability to tune the anisotropic properties by atomic scale control. By separating IMA and BMA with a STO barrier in LSMO/STO/LSMO/NGO magnetic tunneling junctions, we are now able to realize orthogonal magnetization between top and bottom LSMO electrodes (See Supplementary Fig. S5). Furthermore, patterning of the STO buffer layer allows us now also to artificially create in-plane magnetic domains (See Supplementary Fig. S5).

The depth profiles of the magnetization further confirm that IMA arises from the strongly tilted interface structure. The atomic concentration profile and magnetic depth profile in 6 uc LSMO films with and without the STO buffer layer have been probed by resonant X-ray reflectometry (RXR)[36] as shown in Fig. 2d (For details of the RXR experiment, see Supplementary Fig. S6). A depth profile of Mn magnetization (M) can be obtained from the best fit of the asymmetric spectra between left and right circular polarized light. The profiles of Ga, Ti and Mn atomic concentration are shown as well for comparison and indicate an atomic sharp interface with negligible interfacial intermixing. The active magnetic layers in these two samples are all located at the interface region. Our magnetic profiles also reveal the presence of magnetic dead layers near the surface[37] for both buffered and non-buffered LSMO films. The OOC has an impact length scale of ~2 nm and, therefore, could have an influence on the surface part of our ultrathin LSMO films on NGO, which can be excluded for our thicker LSMO films. A more detailed analysis will be performed in a future study. Compared with the non-buffered LSMO, the less distorted buffered LSMO film exhibited a more uniform magnetism due to the reduced structural distortion at the interface as well as a reduced thickness of the dead layer on the surface. This fact could explain the observed enhanced saturated magnetization in buffered LSMO film as shown in Fig. 2a-c. Interestingly, the active magnetic layer in the non-buffered LSMO is the ~3 uc interface region and thus coincident with the strong tilted layer (See bottom panel of Fig. 2d). Therefore, the IMA is correlated to the strong tilted LSMO structure while the BMA is coupled to NNT structure.

The distinct OOR patterns near and far from the interface region, give rise to a sharp transition of the magnetic anisotropy at 8 uc LSMO layer thickness, see Fig. 3. The

contribution from the NNT part to the magnetic anisotropic energy (MAE) will increase

with increasing thickness, hence thicker films (t > 8 uc) exhibit BMA. The strong tilt part

dominates in thinner films with t < 8 uc, hence these films exhibit IMA. At 8 uc, the

competition between IMA and BMA results in biaxial anisotropy with the easy axis along

ab and *–ab* directions. The thickness dependence of LSMO thin films further indicates

that IMA arises from an interfacial NGO-like OOR pattern, while the strain-dominated

NNT part gives rise to BMA.

Concomitant with the magnetic anisotropy, the electronic transport properties in the

LSMO films are found to exhibit anisotropies as well with a sharp transition at a

thickness of 8 uc. Besides a thickness dependent metal insulator transition[38] also an

interfacial OOC driven giant transport anisotropy is observed in LSMO films with

thicknesses of 6 and 7 uc, which exhibit higher electrical conductivities along the *a*-axis,

see Fig. 4a. In thicker films where OOC subsides, the anisotropy becomes much smaller.

No thermal hysteresis is observed in the cooling down and warming up cycles, so that a

possible anisotropic percolation in a phase separation scenario is excluded[11]. Figure 4b

shows the resistivity along two different directions *a* vs *b* at 50 K. Almost 2 orders of

magnitude difference of resistivity between the two directions is observed in the 6 uc

sample, significantly larger than previously reported strain induced transport anisotropy[39]

in LSMO/DyScO$_3$. This difference decreases with increasing thickness, and for t ≥ 8 uc,

this difference is too small to note any anisotropy. However, the temperature dependent

magnetoresistance, MR = (R(B)-R(0))/R(0), in Fig. 4c still reflects the presence of

transport anisotropy in thick films. Both thin film (6 uc) and thick film (12 uc) exhibit

anisotropic MR effect with peak position T_P, which reflects a metal-to-insulator transition

in manganites (See Supplementary Fig. S7). However, the sign of $\Delta T_P=T_p(a)-T_p(b)$ for 6 uc and 12 uc films are opposite. Therefore, there is a switch of transport anisotropy with increasing thickness. As shown in Fig. 4d, the difference ΔT_P is thickness dependent and becomes zero at 8 uc. For t < 8uc, it is reversed and as large as $\Delta T_P = 52$ K for 6 uc LSMO, whereas in films with t > 8 uc, it is only about – 2 K. Since the more conductive axis has higher T_P and based on Fig. 3 and Fig. 4d, we can conclude that the easy axis for electronic transport (more conductive axis) coincides with the magnetic easy axis of the LSMO films. By switching the magnetic easy axis of a 6 uc LSMO film through introducing a STO buffer layer, the transport easy axis is also switched to the b-axis (See Supplementary Fig. S7).

Let us now turn to the mechanism of the thickness driven switch of the anisotropic properties. Since strain does not change with thickness and interfacial intermixing is negligible, the transition of MA with thickness can be expected to correlate with the OOR pattern. Along the a-axis, an in-phase (NGO) and out-of-phase (LSMO) mismatch would cause huge oxygen displacements to retain the connectivity of the oxygen octahedra. Furthermore, the rotation of MnO_6 octahedra along the a-axis causes the bond angle θ along the b-axis to become smaller. While along the b-axis, the OOR pattern for both LSMO and NGO are out-of-phase, the displacement of oxygen atoms necessary to match the substrate is less. As a result, the bond angle along the a-axis is larger than along the b-axis, $\theta(a) > \theta(b)$. Further away from the interface, the OOC effect subsides and the strain dominates, resulting in $\theta(b) > \theta(a)$[40]. Based on the above consideration, a structural evolution of a LSMO film is schematically shown in Fig. 5a. The LSMO film is divided into two regions, the interface OOC driven $b^+a^-c^-$ and the strained induced[40] $a^+b^-c^-$. The

larger rotation along *c*-axis for both regions is due to LSMO in-plane compressive strain, which increases the rotation along *c*-axis to give rise to a smaller in-plane lattice constant[40]. In the cross-over thickness the complete LSMO film can be averagely described by $a^+a^-c^-$ and $\langle\theta(a)\rangle \approx \langle\theta(b)\rangle$. The structure characteristic of LSMO near the interface is expected to cause an anisotropic bandwidth (*w*) according to formula[41]

$w \propto \frac{Cos(\pi-\theta)/2}{d^{3.5}}$ with $w(a) > w(b)$. Further away from the interface region, $\theta(b) > \theta(a)$ leads to $w(b) > w(a)$. The expected changes of anisotropic bond angle and bandwidth are consistent with our observed anisotropic transport properties within the double exchange model[42].

According to Fig. 1b-c, the lattice structure of LSMO films relaxes with thickness and becomes bulk-like at a thickness of about 4 uc. Therefore, in thick LSMO films we expect the presence of two regions: an interface region where the anisotropic properties in each layer change with layer position and a strain dominated bulk region where the anisotropic properties are less dependent on layer position. The uniaxial MAE is described by $E = K_u Cos^2\varphi$ where φ is an in-plane angle relative to *a*-axis. For uniaxial anisotropy $K_u = E(a)-E(b)$ is positive or negative, indicating that the easy axis is the *b* or *a*-axis, respectively; for biaxial anisotropy $K_u = 0$. The total K_u can be expressed by $K_{tot} = \sum_{n=1}^{t} K_u(n)$, where $K_u(n)$ is MAE constant of the *n*th layer. The mean MAE constant $\langle K \rangle$ (= K_{tot}/t), (For measurement of $\langle K \rangle$, see Supplementary Fig. S8), is found to nonlinearly depend on thickness (see Fig. 5b). The $\langle K \rangle$ exhibits clear thickness dependence and a cross-over transition from positive to negative values, which can be observed at 8 uc. In contrast, the K_{tot} is linearly dependent on thickness when t > 8 uc (see Fig. 5b). Therefore, K_{tot} can be rewritten as $K_{tot} = \sum_{n=1}^{t_I} K_u(n) + K_{uB}(t - t_I) =$

$K_{uB}t - c$. Here, t_I is thickness of interface region beyond which the $K_u(n)$ is approximated to be constant K_{uB} and c is a constant. K_{uB} and c, as obtained from linear fitting of K_{tot} vs. t curve at t > 8 uc, are 14.4 μeV/uc and 103.7 μeV/uc, respectively. With these parameters, a critical thickness (t_c), where these sub-layers do not contribute to K_{tot} ($K_{uB}t_c - c = 0$), can be estimated to be 7.2 uc, in good agreement with the observed 8 uc critical thickness for <K> = 0 as determined by the magnetic anisotropy measurements.

To understand the microscopic origin of the MA and the expected coupling between transport and magnetic anisotropy, we construct by means of density functional theory (DFT) a tight binding Hamiltonian of LSMO ultrathin films: $\sum_R t_{\alpha\beta}(\vec{R}) e^{i\vec{K}\cdot\vec{R}} + \left(\frac{\lambda}{2}\right)\sigma(\theta,\varphi) + \xi L \cdot S$, including exchange splitting λ and spin-orbit coupling ξ (See Supplementary Fig. S9 and S10). Here, $t_{\alpha\beta}(\vec{R})$ represents the hopping integral from orbital α at site 0 to orbital β at site $\vec{R}$. The structural change due to OOC and strain mainly affects the $t_{\alpha\beta}(\vec{R})$, which in turn leads to a change of the MAE. The hopping terms $t_{\alpha\beta}(\vec{R})$ can be qualitatively indicated by the transport properties in our experiment. We therefore simply mimic the structural and transport anisotropy by introducing anisotropic hopping terms[42] parametrized by A_t: $t_0(\vec{a})$ and $t_0(\vec{b}) = t_0(\vec{a})(1 - A_t)$ along $\vec{a}$ and $\vec{b}$ respectively. The calculation of the MAE indicates an in-plane easy axis for a monolayer LSMO film (See Supplementary Fig. S10), while the easy axis in the *ab*-plane depends on the asymmetric hopping factor A_t (see Fig. 5c). In the case of an isotropic in-plane structure ($A_t = 0$), a biaxial anisotropy with easy axis [110]$_{pc}$ is obtained consistent with observations in (001) LSMO films on cubic STO and

$(LaAlO_3)_{0.3}(Sr_2AlTaO_6)_{0.7}$ substrates (see Supplementary Fig. S11). If $t_0(\vec{a})$ is 0.5%

percent higher than $t_0(\vec{b})$ (A_t = 0.5%), the easy axis is rotated from the *ab* direction to

the *a*-axis and the film becomes uniaxially anisotropic, while A_t = -0.5% will switch the

easy axis to the *b*-axis. Thus the easy axis prefers to align along the axis with the largest

hopping amplitude, which is also the axis for the largest conductivity as in experiment.

The calculated in-plane anisotropic energy is of the order of 4 μeV/uc, qualitatively

consistent with the experimental observations.

In conclusion, OOC driven magnetic and transport anisotropies are realized in
LSMO/NGO heterostructures. Competition between the interfacial OOC and the strain
further away from the interface leads to a thickness driven sharp transition of the
anisotropic properties. The observed coupling of transport and magnetic anisotropy as
well as the tight-binding modeling indicate the key role of the anisotropic bandwidth for
the anisotropic properties in LSMO. Our finding will also provide new insight into the
recently reported strain driven transport anisotropy in manganite films[11,39,42]. The
observed OOC can be extended into other perovskite oxide heterostructures or
superlattices. Furthermore, the revealed competition between OOC and strain which
results in thickness dependent properties should have significant impact on the
understanding of widely reported reduced dimensionality effect in many correlated
perovskite ultrathin films.

Our results unequivocally link the atomic structure near interfaces to macroscopic
properties. The strong correlation between controllable oxygen network and
functionalities will have significant impact on both fundamental research and
technological application of correlated perovskite heterostructures. By controlling

interfacial OOC, we are now able to pattern in 3 dimensions the magnetization to achieve non-collinear magnetization in both in-plane and out of plane directions, thus making the heterostructures promising for application in orthogonal spin transfer devices, spin oscillators and low field sensors. Moreover, one could extend the revealed competition between strain and OOC to a new direction to realize piezoelectric control of magnetization reversal for spintronics application by tuning balance between those two co-existent effects.

Methods

LSMO thin films were grown on atomically flat NGO (110) substrates from a stoichiometric $La_{2/3}Sr_{1/3}MnO_3$ target by pulsed laser deposition using a KrF excimer laser operating at 248 nm. The atomically flat NGO substrate, as confirmed by atomic force microscopy (AFM), was obtained by BHF chemical etching and subsequent annealing at 1050 $^{\circ}$C for 4 hours[33]. The laser fluence and repetition rate were 0.6 J/cm^2 and 2 Hz respectively. The oxygen partial pressure and substrate temperature were maintained at 0.2 mBar and 680 $^{\circ}$C respectively during the growth. The growth process was monitored by reflection high-energy electron diffraction (RHEED), which confirmed the layer by layer characteristic growth.

Scanning transmission electron microscopy (STEM) was performed on the X-Ant-Em instrument at the University of Antwerp. Cross-sectional cuts of the samples along the [1-10] direction were prepared using a FEI Helios 650 dual-beam Focused Ion Beam device. The 6uc LSMO film was capped with a 10 nm STO layer grown at room temperature in order to prevent LSMO ultrathin layer from damage during the preparation of TEM cross-section specimen in both buffered and un-buffered cases. Satisfactory samples were prepared using very low energy ion beam thinning subsequent to a protection of the sample surface by sputtering of a 10nm thick carbon protection layer, followed be E-beam deposition of Platinum as a first step to the FIB lamella preparation procedure. The Electron Microscope used consists of an FEI Titan G3 electron microscope equipped with an aberration corrector for the probe-forming lens as well as a high-brightness gun and a Super-EDX 4-quadrant detector operated at 300 kV acceleration voltage for the EDX experiments and STEM-ADF and ABF imaging. The STEM convergence semi-angle

used was 21 mrad, providing a probe size of ~0.8 Å. The collection semi-angle ranges from 11-29 mrad and 29-160 mrad for ABF and ADF imaging respectively.

Magnetic and transport properties were measured by using a Quantum Design Vibration Sample Magnetometer (VSM) and a Physical Properties Measurement System (PPMS) respectively. The magnetization of the LSMO films was acquired by subtracting the paramagnetic signal of each NGO substrate (See Supplementary Fig. S12). The transport properties were analyzed in a van-der-Pauw geometry, in which the resistances along a and b-axis were measured simultaneously.

The magneto-optical profile was measured using x-ray resonant magnetic reflectivity (XRMR)[43]. The XRMR experiments were performed using an in-vacuum 4-circle diffractometer at the Resonant Elastic and Inelastic X-ray Scattering (REIXS) beamline of the Canadian Light Source (CLS) in Saskatoon, Canada[44]. The beamline has a flux of 5×10^{12} photon/s and photon energy resolution $\Delta E/E$ of $\sim 10^{-4}$. The base pressure of the diffractometer chamber was kept lower than 10^{-9} Torr. The samples were aligned with their surface normal in the scattering plane and measured at a temperature of 20 K. The measurements were carried out in the specular reflection geometry with several nonresonant photon energies as well as energies at the Mn $L_{2,3}$ resonance (~635-660 eV). For details about the magneto-optical profile extraction, see Supplementary Fig. S6.

A DFT based tight binding Hamiltonian was constructed to calculate the MAE of LSMO ultrathin films, $H(\vec{k}) + \left(\frac{\lambda}{2}\right)\sigma(\theta,\varphi) + \xi L \cdot S$. The first term $H(\vec{k})$, paramagnetic tight binding Hamiltonian, is constructed on Wannier basis projected from DFT calculated Bloch waves of LSMO near Fermi level. The Wannier projection was performed with

Wien2Wannier package, employing Wannier90 for constructing maximally localized Wannier orbitals[45]. The second term $\left(\frac{\lambda}{2}\right)\sigma(\theta,\varphi)$ leads to an exchange splitting λ for spins parallel and antiparallel to (θ, φ) direction. We set $\lambda = 2eV$ which is the typical exchange splitting in manganites[46]. The last term is the atomic spin orbit coupling of Mn d orbitals with $\xi = 0.05$ eV. A very fine k mesh (e.g. $160 \times 160 \times 160$) was used to make sure that the total energy converges down to 10^{-3} μeV accuracy.

References:

[1] Brataas, A., Kent, A.D. and Ohno, H., Current-induced torques in magnetic materials, *Nature Mater.* **11**, 372 (2012).

[2] Brataasa, A., Bauer, G.E.W. and Kelly, P.J., Non-collinear magnetoelectronics, *Phys. Rep.* **427**, 157 (2006).

[3] Hwang, H.Y., Iwasa, Y., Kawasaki, M., Keimer, B., Nagaosa, N. & Tokura, Y., Emergent phenomena at oxide interfaces, *Nature Mater.* **11**, 103 (2012).

[4] Zubko, P., Gariglio, S., Gabay, M., Ghosez, P. & Triscone, J.-M., Interface Physics in Complex Oxide Heterostructures, *Annu. Rev. Condens. Matter Phys.* **2**, 141 (2011).

[5] Chakhalian, J., Freeland, J.W., Habermeier, H.-U., Cristiani, G., Khaliullin, G., van Veenendaal, M. & Keimer, B., Orbital reconstruction and covalent bonding at an oxide interface, *Science* **318**, 1114–1117 (2007).

[6] Ohtomo, A. & Hwang, H.Y., A high-mobility electron gas at the $LaAlO_3$/$SrTiO_3$ heterointerface, *Nature* **427**, 423 (2004).

[7] Brinkman, A., Huijben, M., van Zalk, M., Huijben, J., Zeitler, U., Maan, J.C., van der Wiel, W.G., Rijnders, G., Blank, D.H.A. & Hilgenkamp, H., Magnetic effects at the interface between non-magnetic oxides, *Nature Mater.* **6**, 493 - 496 (2007).

[8] Tokura, Y. & Nagaosa, N., Orbital physics in transition-metal oxides, *Science* **288**, 462 (2000).

[9] Dagotto, E., Complexity in strongly correlated electronic systems, *Science* **309**, 257 (2005).

[10] Aetukuri, N.B., Gray, A.X., Drouard, M., Cossale, M., Gao, L., Reid, A.H., Kukreja, R., Ohldag, H., Jenkins, C.A., Arenholz, E., Roche, K.P., Dürr, H.A., Samant, M.G. & Parkin, S.P., Control of the metal–insulator transition in vanadium dioxide by modifying orbital occupancy, *Nature Phys.* **9**, 661 (2013).

[11] Ward, T.Z., Budai, J.D., Gai, Z., Tischler, J.Z., Yin, L. & Shen, J., Elastically driven anisotropic percolation in electronic phase-separated manganites, *Nature Phys.* **5**, 885 (2009).

[12] Schlom, D.G., Chen, L.-Q., Eom, C.-B., Rabe, K.M., Streiffer, S.K. & and Triscone, J.-M., Strain tuning of ferroelectric thin films, *Ann. Rev. Mater. Res.* **37**, 589 (2007).

[13] Boris, A.V., Matiks, Y., Benckiser, E., Frano, A., Popovich, P., Hinkov, V., Wochner, P., Castro-Colin, M., Detemple, E., Malik, V.K., Bernhard, C., Prokscha, T., Suter, A., Salman, Z., Morenzoni, E., Cristiani, G., Habermeier, H.-U. & Keimer, B., Dimensionality control of electronic phase transitions in nickel-oxide superlattices, *Science* **332**, 937 (2011).

[14] King, P.D.C, Wei, H.I., Nie, Y.F., Uchida, M., Adamo, C., Zhu, S., He, X., Božović, I., Schlom, D.G., Shen, K.M., Atomic-scale control of competing electronic phases in ultrathin $LaNiO_3$, *Nat. NanoTech.* **9**, 443 (2014).

[15] Salamon, M.B. & Jaime, M., The physics of manganites: Structure and transport, *Rev. Mod. Phys.* **73**, 583 (2001).

[16] Coey, J.M.D., Viret, M. & von Molnaír, S., Mixed-valence manganites, *Adv. Phys.* **48**, 167 (1999).

[17] Chmaissem, O., Dabrowski, B., Kolesnik, S., Mais, J., Brown, D.E., Kruk, R., Prior, P., Pyles, B. & Jorgensen, J.D., Relationship between structural parameters and the Néel temperature in $Sr_{1-x}Ca_xMnO_3$ ($0<\sim x<\sim 1$) and $Sr_{1-y}Ba_yMnO_3$ ($y<\sim 0.2$), *Phys. Rev. B* **64**, 134412 (2001).

[18] Radaelli, P.G., Iannone, G., Marezio, M., Hwang, H.Y., Cheong, S.-W., Jorgensen, J.D. & Argyriou, D.N., Structural effects on the magnetic and transport properties of perovskite $A_{1-x}A'_xMnO_3$ (x = 0.25, 0.30), *Phys. Rev. B* **56**, 8265 (1997).

[19] Alonso, J.A., Martínez-Lope, M.J., Casais, M.T., Aranda, M.A.G. & Fernández-Díaz, M.T., Metal-insulator transitions, structural and microstructural evolution of $RNiO_3$ (R = Sm, Eu, Gd, Dy, Ho, Y) perovskites: Evidence for room-temperature charge disproportionation in monoclinic $HoNiO_3$ and $YNiO_3$, *J. Am. Chem. Soc.* **121**, 4754 (1999).

[20] Garcia-Munoz, J.L., Fontcuberta, J., Suaaidi, M. & Obradors, X., Bandwidth narrowing in bulk $L_{2/3}A_{1/3}MnO_3$ magnetoresistive oxides, *J. Phys.: condens. Matter* **8**, L787 (1996).

[21] Ding, Y., Haskel, D., Tseng, Y.-C., Kaneshita E., van Veenendaal, M., Mitchell, J.F., Sinogeikin, S.V., Prakapenka, V. & Mao, H.-K., Pressure-induced magnetic transition in manganite ($La_{0.75}Ca_{0.25}MnO_3$), *Phys. Rev. Lett.* **102**, 237201 (2009).

[22] Zhai, X.F., Cheng, L., Liu, Y., Schlepütz, C.M., Dong, S., Li, H., Zhang, X.Q., Chu, S.Q., Zheng, L.R, Zhang, J., Zhao, A.D., Hong, H., Bhattacharya, A., Eckstein, J.N., Zeng, C.G., Correlating interfacial octahedral rotations with magnetism in $(LaMnO_{3+\delta})_N/(SrTiO_3)_N$ superlattices, *Nat. Commun.* **5,** 4283 (2014).

[23] Rondinelli, J.M. & Spaldin, N.A., Structure and properties of functional oxide thin films: Insights from electronic-structure calculations, *Adv. Mater.* **23**, 3363 (2011).

[24] Lee, J.H., Luo, G., Tung, I.C., Chang, S.H., Luo, Z., Malshe, M., Gadre, M., Bhattacharya, A., Nakhmanson, S.M., Eastman, J.A., Hong, H., Jellinek, J., Morgan, D., Fong, D. & Freeland, J.W., Dynamic layer rearrangement during growth of layered oxide films by molecular beam epitaxy, *Nature Mater.* **13**, 879 (2014).

[25] Rondinelli, J.M., May, S.J. & Freeland, J.W., Control of octahedral connectivity in perovskite oxide heterostructures: An emerging route to multifunctional materials discovery, *MRS Bull.* **37**, 261 (2012).

[26] Kinyanjui, M.K., Lu, Y., Gauquelin, N., Wu, M., Frano, A., Wochner, P., Reehuis, M., Christiani, G., Logvenov, G., Habermeier, H.-U., Botton, G.A., Kaiser, U., Keimer, B. & Benckiser, E., Lattice distortions and octahedral rotations in epitaxially strained $LaNiO_3/LaAlO_3$ superlattices, *Appl. Phys. Lett.* **104**, 221909 (2014).

[27] Borisevich, A.Y., Chang, H.J., Huijben, M., Oxley, M.P., Okamoto, S., Niranjan, M.K., Burton, J.D., Tsymbal, E.Y., Chu, Y.H., Yu, P., Ramesh, R., Kalinin, S.V. & and Pennycook, S.J., Suppression of octahedral tilts and associated changes in electronic

properties at epitaxial oxide heterostructure interfaces, *Phys. Rev. Lett.* **105**, 087204 (2010).

[28] He, J., Borisevich, A.Y., Kalinin, S.V., Pennycook, S.J. & Pantelides, S.T., Control of octahedral tilts and magnetic properties of perovskite oxide heterostructures by substrate symmetry, *Phys. Rev. Lett.* **105**, 227203 (2010).

[29] Aso, R., Kan, D., Shimakawa, Y. & Kurata, H., Atomic level observation of octahedral distortions at the perovskite oxide heterointerface, *Sci. Rep.* **3**, 2214 (2013).

[30] Chen, Y.B, Sun H.P., Katz, M.B., Pan X.Q., Choi, K.J., Jang, H.W and Eom, C.B., Interface structure and strain relaxation in $BaTiO_3$ thin films grown on $GdScO_3$ and $DyScO_3$ substrates with buried coherent $SrRuO_3$ layer, *Appl. Phys. Lett.* **91**, 252906 (2007).

[31] Glazer, A.M., Classification of tilted octahedral in perovskites, *Acta Crystallogr., Sect. B: Struct. Sci.* **28**, 3384 (1972).

[32] Vasylechko, L., Akselrud, L., Morgenroth, W., Bismayer, U., Matkovskii, A. & Savytskii, D., The crystal structure of $NdGaO_3$ at 100 K and 293 K based on synchrotron data, *J. Alloys Compd.* **297**, 46 (2000).

[33] Liao, Z., Huijben, M., Koster, G. & Rijnders, G., Uniaxial magnetic anisotropy induced low field anomalous anisotropic magnetoresistance in manganite thin films, *Appl. Phys. Lett. Mater.* **2**, 096112 (2014).

[34] Ovsyannikov, S.V., Abakumov, A.M., Tsirlin, A.A, Schnelle, W., Egoavil, R., Verbeeck, J., Tendeloo, G.V., Glazyrin, K.V., Hanfland, M. & Dubrovinsk, L, Perovskite-like Mn_2O_3: a path to new manganites, *Angew. Chem. Int. Ed*. **52**, 1494 (2013).

[35] Boschker, H., Mathews, M., Houwman, E.P., Nishikawa, H., Vailionis, A., Koster, G., Rijnders, G. & Blank, D.H.A., Strong uniaxial in-plane magnetic anisotropy of (001)- and (011)-oriented $La_{0.67}Sr_{0.33}MnO_3$ thin films on $NdGaO_3$ substrates, *Phys. Rev. B* **79**, 214425 (2009).

[36] Macke, S., Radi, A., Hamann-Borrero, J.E, Verna, A., Bluschke, M., Brück, S., Goering E., Sutarto, R., He, F.Z., Cristiani, G., Wu, E., Benckiser, E., Habermeier, H.U., Logvenov, G., Gauquelin, N., Botton, G.A., Kajdos, A.P., Stemmer, S., Sawatzky, G.A., Haverkort, M.W., Keimer, K., and Hinkov, V., Element specific monolayer depth profiling, *Adv. Mater.* **26**, 6554 (2014).

[37] Park, J.H., Vescovo, E., Kim, H.J., Kwon, C., Ramesh, R., and Venkatesan, T., Magnetic properties at surface boundary of a half-metallic ferromagnet $La_{0.7}Sr_{0.3}MnO_3$, *Phys. Rev. Lett.* **81**, 1953 (1998).

[38] Huijben, M., Martin, L.W., Chu, Y.-H., Holcomb, M.B., Yu, P., Rijnders, G., Blank, D.H.A., and Ramesh, R., Critical thickness and orbital ordering in ultrathin $La_{0.7}Sr_{0.3}MnO_3$ films, Phys. Rev. B 78, 094413 (2008).

[39] Wang, B.M, You, L., Ren, P., Yin, X.M., Peng, Y., Xia, B., Wang, L., Yu, X.J., Poh, S.M., Yang, P., Yuan, G.L., Chen, L., Rusydi, A., and Wang, J.L., Oxygen-driven anisotropic transport in ultra-thin manganite films, *Nat. Commun*. **4**, 2778 (2013).

[40] Vailionis, A., Boschker, H., Siemons, W., Houwman, E.P., Blank, D.H.A., Rijnders, G. & Koster, G., Misfit strain accommodation in epitaxial ABO_3 perovskites: lattice rotations and lattice modulations, *Phys. Rev. B* **83** (6), 064101(2011).

[41] Medarde, M., Mesot, J., Lacorre, P., Rosenkranz, S., Fischer, P. & Gobrecht, K., High-pressure neutron-diffraction study of the metallization process in $PrNiO_3$, *Phys. Rev. B* **52**, 9248 (1995).

[42] Dong, S., Yunoki, S., Zhang, X., Şen, C., Liu, J.-M. & Dagotto, E., Highly anisotropic resistivities in the double-exchange model for strained manganites, *Phys. Rev. B* **82**, 159902 (2010).

[43] Macke, S. & Goering, E., Magnetic reflectometry of heterostructures, *J. Phys.: Conden.s Matter* **26**, 363201, (2014).

[44] Hawthorn, D.G., He, F., Venema, L., Davis, H., Achka, A.J., Zhang, J., Sutarto, R., Wadati, H., Radi, A., Wilson, T., Wright, G., Shen, K.M., Geck, J., Zhang, H., Novák, V. and Sawatzky, G.A., An in-vacuum diffractometer for resonant elastic soft x-ray scattering, *Rev. of Sci. Instrum.* **82**, 073104 (2011).

[45] Zhong, Z., Toth, A. & Held, K., Theory of spin-orbit coupling at $LaAlO_3/SrTiO_3$ interfaces and $SrTiO_3$ surfaces, *Phys. Rev. B* **87**, 161102 (2013).

[46] Yamasaki, A., Feldbacher, M., Yang, Y.-F., Andersen, O.K. & Held K., Pressure-induced metal-insulator transition in $LaMnO_3$ is not of Mott-Hubbard type, *Phys. Rev. Lett.* **96**, 166401 (2006).

Acknowledgements

Author Contributions

Z.L. concept design, film growth and magnetic/transport measurements. Data analysis and interpretation: Z.L., M.H., G.K., G.R., Z.Z; STEM and EDX measurements and analysis: N.G., S.V.A., J.V., G.V.T; RXR measurements and analysis: S. M., G. K., R.J.G., G.A.S.; DFT calculations: Z.Z., K.H; All authors extensively discussed the results and were involved in writing of the manuscript.

Additional information

Supplementary information is available in the online version of the paper. Reprints and permissions information is available online at www.nature.com/reprints. Correspondence and requests for materials should be addressed to M.H.

Competing financial interest

The authors declare no competing financial interests.

Figures and Figure captions:
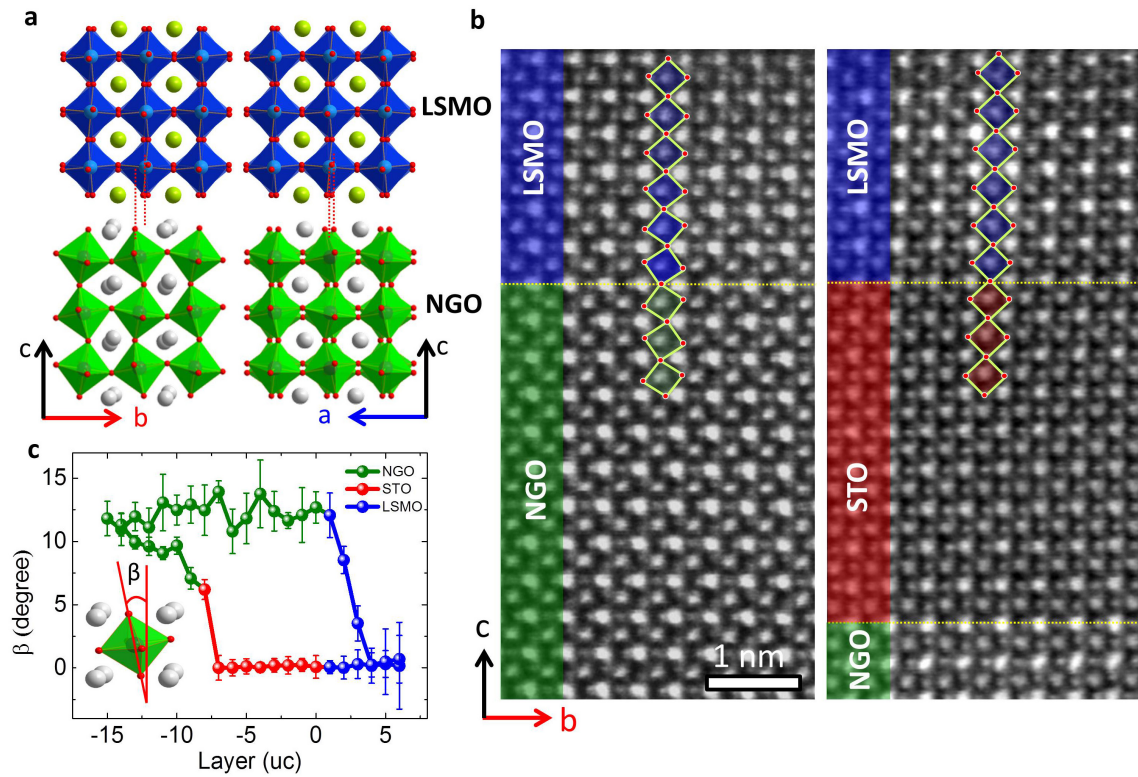
Figure 1 | Oxygen octahedral coupling at interfaces in manganite heterostructures. a, Schematic models of atomic ordering in LSMO and NGO crystal structures. **b**, Inversed annular bright-field STEM images of LSMO/NGO (left) and LSMO/STO/NGO (right) heterostructures. The oxygen atoms are clearly visible, and the connectivity of oxygen octahedra across the interfaces is indicated. The MnO_6 octahedra shows a clear in-phase rotation following the NGO. The LSMO films are 6 uc thick while the STO buffer layer has a thickness of 9 uc. **c**, Layer-position dependent octahedral tilt angle (β) in LSMO/NGO heterostructures with and without a STO buffer layer.
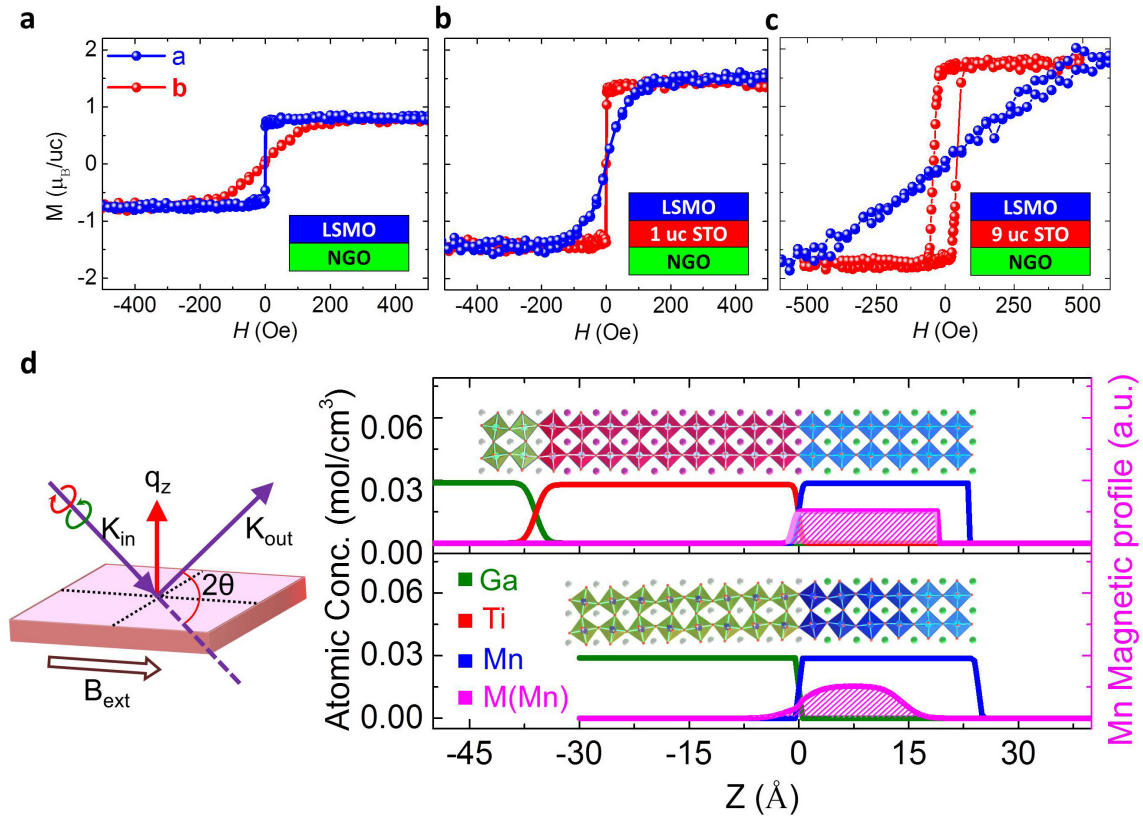
Figure 2 | Magnetic anisotropy in manganite heterostructures. The M-H curves at 100 K along *a* and *b*-axis of the 6 uc LSMO films on NGO substrates without (**a**) and with a 1 uc (**b**) and 9 uc (**c**) STO buffer layer. **d,** RXR measurements of 6 uc LSMO films with (top panel) and without (bottom panel) a 9 uc STO buffer layer showing depth profiles of the Ga, Ti, Mn atomic concentration (resp. green, red and blue lines) and Mn magnetization (M, purple line with shaded area) at 20 K. Schematic shows experimental setup to perform RXR measurement where a 0.6 T magnetic field was applied in-plane along magnetic easy axis during the measurement. Atomic structure profiles along out of plane direction (Z), according to Fig. 1b-c, are also shown for comparison.
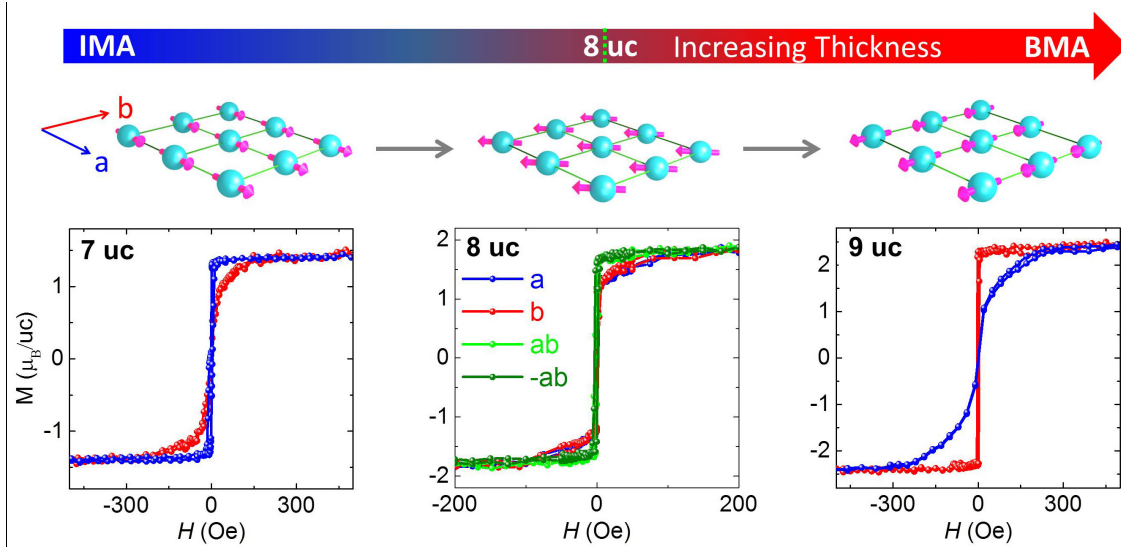
Figure 3 | Thickness dependence of the magnetic anisotropy in manganite heterostructures. The M-H curves at 100 K along *a* and *b*-axis of the LSMO films with thicknesses of 7, 8 and 9 uc on NGO substrates. The schematics at the top show the corresponding ground state of the Mn spin orientation.
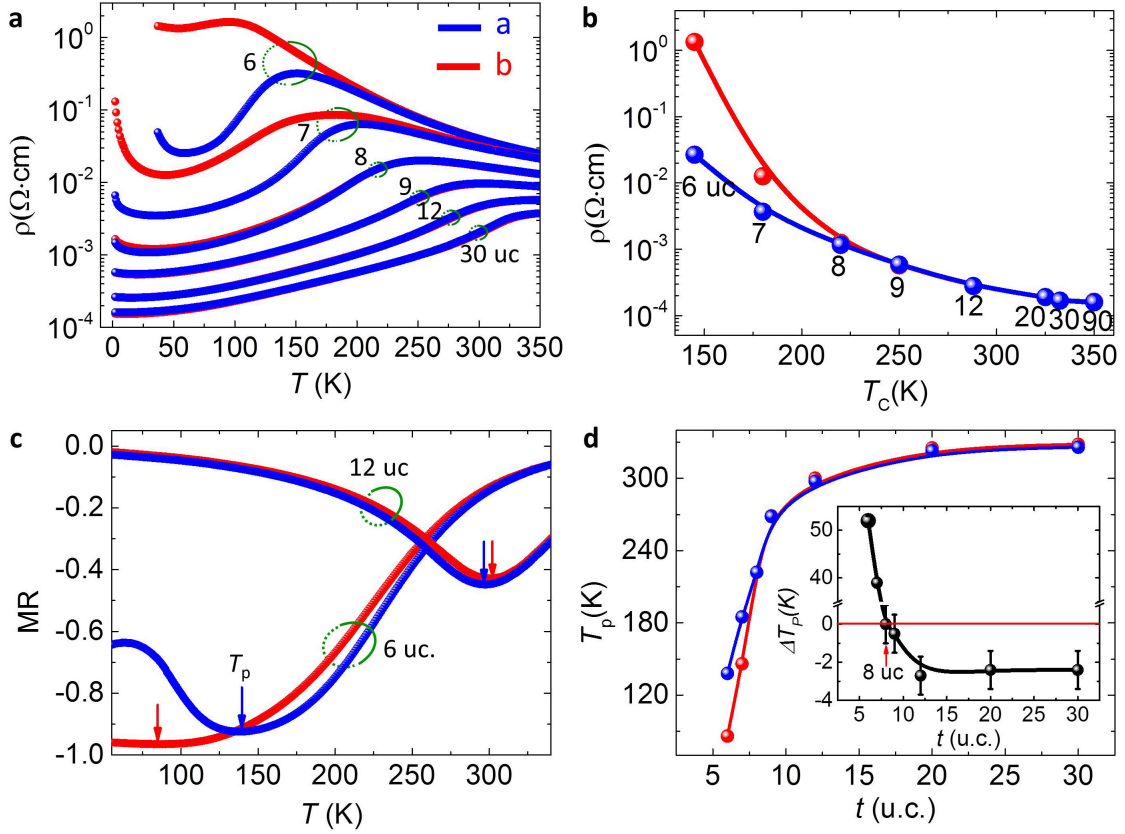
Figure 4 | Thickness dependence of the transport anisotropy in manganite heterostructures. a, Temperature dependent resistivity along *a* and *b*-axis for different LSMO thickness from 6 to 30 uc. **b**, Curie temperature dependent resistivity at 50 K along the *a* and *b*-axis. The corresponding thickness is marked at each data point. **c**, Temperature dependent magnetoresistance MR=(R(B)-R(0))/R(0) along *a* and *b*-axis under out of plane 9 T magnetic field for 6 and 12 uc LSMO films. **d**, T_p versus LSMO film thickness along *a* and *b*-axis. Inset, $\Delta T_p = T_p(a) - T_p(b)$ versus LSMO film thickness. Data measured along the *a*-axis is indicated in blue in all 4 figures, while data along *b*-axis is indicated in red.
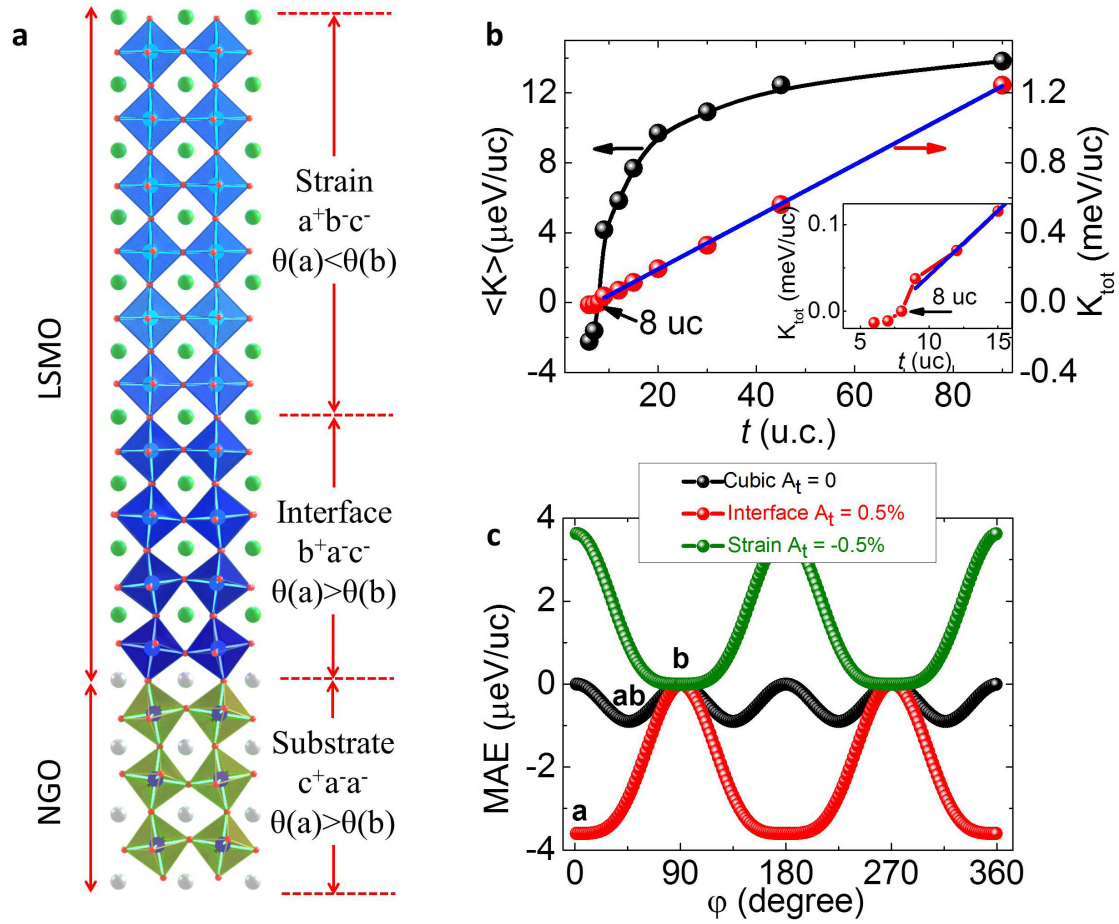
Figure 5 | Structural mechanism of directional switching of magnetic anisotropy. a, Structural evolution along the out-of-plane direction of the LSMO thin film on a NGO substrate. **b**, Film thickness dependence of the anisotropic energy constant $<K>$ and total anisotropic energy constant K_{tot} at 50 K. Inset: Zoom in around t = 8 uc. **c**, Tight binding simulations of the anisotropy energy of a LSMO monolayer with different asymmetric hopping factor A_t ($= 1 - t_0(\vec{b})/t_0(\vec{a})$): 0% (cubic LSMO, black), 0.5% (interfacial LSMO on NGO, red), -0.5% (strained bulk LSMO on NGO, green).